Few-Layered SnS_2 on Few-Layered Reduced Graphene Oxide as Na-Ion Battery Anode with Ultralong Cycle Life and Superior Rate Capability

Yandong Zhang, Peiyi Zhu, Liliang Huang, Jian Xie, Shichao Zhang, Gaoshao Cao, and Xinbing Zhao*

Na-ion Batteries have been considered as promising alternatives to Li-ion batteries due to the natural abundance of sodium resources. Searching for high-performance anode materials currently becomes a hot topic and also a great challenge for developing Na-ion batteries. In this work, a novel hybrid anode is synthesized consisting of ultrafine, few-layered SnS_2 anchored on few-layered reduced graphene oxide (rGO) by a facile solvothermal route. The SnS_2/rGO hybrid exhibits a high capacity, ultralong cycle life, and superior rate capability. The hybrid can deliver a high charge capacity of 649 mAh g^{-1} at 100 mA g^{-1}. At 800 mA g^{-1} (1.8 C), it can yield an initial charge capacity of 469 mAh g^{-1}, which can be maintained at 89% and 61%, respectively, after 400 and 1000 cycles. The hybrid can also sustain a current density up to 12.8 A g^{-1} (≈28 C) where the charge process can be completed in only 1.3 min while still delivering a charge capacity of 337 mAh g^{-1}. The fast and stable Na-storage ability of SnS_2/rGO makes it a promising anode for Na-ion batteries.

1. Introduction

Currently, Na-ion batteries have received an increasing attention as promising alternatives to Li-ion batteries because of the natural abundance of sodium element.[1–5] One of the challenges to commercialize Na-ion batteries is to develop suitable anode materials since the large size of Na ions precludes their intercalation into graphite,[6,7] unlike the case for Li ions. Although other forms of carbon materials, such as hard carbon[8–12] and carbon nanofibers/nanowires[13,14] are electrochemically more active towards Na storage, their capacities are not satisfactory. Recent work has shown that Na-storage capacity over 300 mAh g^{-1} can be achieved in N-doped porous carbon nanosheets,[15] reduced graphene oxide (rGO),[16] hard carbon from sugar,[17] porous carbon nanofibers,[18] and bio-derived carbon.[19,20] Lotfabad et al. reported a novel bio-derived carbon material with excellent Na-storage properties: a high capacity of 355 mAh g^{-1} after 10 cycles at 50 mA g^{-1}, a flat plateau capacity of ≈200 mAh g^{-1} below 0.1 V at 50 mA g^{-1}, and a stable cycling with 88% capacity retention over 290 cycles at 100 mA g^{-1}.[20] The large graphene interlayer spacing of this pseudographitic carbon allows for facile Na ions intercalation/de-intercalation between the layers, similar to the case for graphite in Li-ion batteries.

Another method to obtain high capacity is to use materials with a Na-alloying/de-alloying mechanism, typically, Sb[21–26] or Sn[27–33] based materials. The theoretical Na-storage capacities of metallic Sb and Sn reach 660 and 847 mAh g^{-1}, respectively, by forming Na-rich Na_3Sb[21] and $Na_{15}Sn_4$[34,35] compositions. For example, a fiber-like Sb/C composite could yield a capacity of 337 mAh g^{-1} at 3000 mA g^{-1} and keep a high capacity retention of 90% after 400 cycles at 200 mA g^{-1}.[26] A Sn–SnS–C composite could maintain a capacity of 407 mAh g^{-1} after 150 cycles at 100 mA g^{-1}.[30] The work by Farbod et al. showed that Sn–Ge–Sb thin film alloys could exhibit promising Na-storage performance.[31] The alloy with $Sn_{50}Ge_{25}Sb_{25}$ composition could deliver a high initial capacity of 833 mAh g^{-1} at 85 mA g^{-1}, maintain a capacity of 662 mAh g^{-1} after 50 cycles, and yield a stable capacity of 381 mAh g^{-1} at a current as high as 8500 mA g^{-1}. Usually, to obtain a high and stable Na-storage capacity, a dispersing matrix, for instance carbon material, is necessary to buffer the large volume changes upon sodiation/de-sodiation, and to provide conducting networks. The large volume changes upon cycling have been verified by in situ observation technique.[36] Among various carbon materials, graphene has received a special interest as an ideal matrix for Na-storage hosts,[37–40] due to its unique properties including large specific surface area,[41] high mechanical strength,[42] and superior electronic conductivity.[43]

Y. D. Zhang, Dr. J. Xie, Prof. X. B. Zhao
State Key Laboratory of Silicon Materials
Department of Materials Science and Engineering
Zhejiang University
Hangzhou 310027, P. R. China
E-mail: xiejian1977@zju.edu.cn
Dr. P. Zhu
Industrial Technology Research Institute
of Zhejiang University
Hangzhou 310058, P. R. China
L. Huang, Dr. J. Xie, Dr. G. S. Cao, Prof. X. B. Zhao
Key Laboratory of Advanced Materials and
Applications for Batteries of Zhejiang Province
Hangzhou 310027, P. R. China
Prof. S. C. Zhang
School of Materials Science and Engineering
Beijing University of Aeronautics and Astronautics
Beijing 100191, P. R. China
DOI: 10.1002/adfm.201402833

Recently, some layered transition metal disulfides, such as MoS_2,[44–48] WS_2[49–53] and SnS_2,[54–59] have received an increasing attention because of their high Li or Na-storage capacities. Both Na and Li-storage properties of these layered materials can be obviously improved by graphene incorporation. In these disulfides, the Na storage of MoS_2 and WS_2 is realized through the conversion reactions:

$$MoS_2+4Na \leftrightarrow 2Na_2S+Mo \quad (1)$$

$$WS_2+4Na \leftrightarrow 2Na_2S+W \quad (2)$$

which are different from the intercalation/de-intercalation mechanism for carbon materials[20] and alloying/de-alloying mechanism for Sb or Sn based materials.[21–33] For SnS_2, it demonstrates a combined conversion and alloying/de-alloying mechanism through the reactions:[58]

$$SnS_2+4Na \leftrightarrow Sn+2Na_2S \quad (3)$$

$$Sn + 3.75Na \leftrightarrow Na_{3.75}Sn(Na_{15}Sn_4) \quad (4)$$

where the conversion reaction (3) is generally considered to be irreversible, while the alloying/de-alloying reactions provide the reversible Na-storage capacity. Interestingly, Recent work by Zhou et al. has shown that layered SnS, transformed from layered SnS_2, exhibits reversible reactions in both conversion and alloying/de-alloying processes.[58] The SnS/graphene composite could yield a high capacity of 940 mAh g^{-1} and a superior rate capability of 492 and 308 mAh g^{-1} after 250 cycles at 810 and 7290 mA g^{-1}, respectively.

Compared with others, layered materials offer some advantages for Na storage. First, layered materials tend to form two-dimensional (2D) sheet-like structure, which is structurally compatible with 2D graphene; second, the stacking of layered materials in the c-direction can be inhibited through the interaction with the second component, for example graphene oxide (GO),[56,58] due to the weak van der Waals forces between layers, which can be utilized to reduce the thickness of the sheet-like materials, thus shortening the diffusion length of Na ions;[58] third, layered structure with a large interlayer spacing (for example c = 0.59 nm for SnS_2) facilitates the insertion/extraction of Na ions and is more tolerant to cycling-induced volume changes. It is thus anticipated that the accessibility of Na ions should be enhanced by decreasing both the thickness and lateral size of the layered materials.

In this work, we synthesized a SnS_2/rGO nanohybrid with plate-on-sheet structure by a facile solvothermal route. Small size in both the thickness (<4 nm) and lateral (<10 nm) directions can be realized by this facile route without adding any additive or surfactant during the synthesis. The small lateral size and ultrathin feature of SnS_2 as well as the unique plate-on-sheet structure endow SnS_2/rGO with a high capacity, excellent high-rate cycling stability and superior rate capability. The hybrid can deliver a high charge capacity of 649 mAh g^{-1} at 0.1 A g^{-1}. A chare capacity of 337 mAh g^{-1} is still retained at a current density as high as 12.8 A g^{-1} (≈28 C), namely, 128-fold current increase compared with 0.1 A g^{-1}. After 300 cycles at 200 mA g^{-1}, the hybrid can deliver a charge capacity of 509 mAh g^{-1}, with high capacity retention of ≈86%. The hybrid can also endure high-rate (800 mA g^{-1}) and long-term (1000 cycles) cycling with a charge capacity close to 300 mAh g^{-1} retained. Ex situ structural characterization and impedance analysis confirm that besides the unique architecture, the formation of a stable and thin surface film also contributes to the outstanding performance of SnS_2/rGO.

2. Results and Discussion

Figure 1a shows the X-ray diffraction (XRD) patterns of SnS_2/rGO, SnS_2 and rGO. All the diffraction peaks of SnS_2 can be assigned to the hexagonal SnS_2 (JCPDS Card no.23–0677). The broad peak at around $2\theta = 25°$ in SnS_2/rGO and rGO is the (002) peak of rGO. The appearance of this peak indicates the reduction of GO. The broad (002) peak suggests that the rGO is full of effects, such as divancancies and Stone-Wales.[20] This is supported by Raman spectroscopy (Figure S1, Supporting Information), where the intensity ratio of G-mode and D-mode, I_G/I_D, is calculated to be only 0.79. The content of rGO in SnS_2/rGO is calculated to be 19 wt% by a combined thermogravimetric (TG) analysis on SnS_2/rGO and SnS_2 (Figure S2, Supporting Information). The broad diffraction peaks of SnS_2 suggest the small size of SnS_2. The X-ray photoelectron spectroscopy (XPS) survey in Figure 1b detects expected Sn, S, C and O elements in SnS_2/rGO. The peaks at 486.6 and 495.1 eV in Figure 1c correspond to the $Sn3d_{5/2}$ and $Sn3d_{3/2}$ of Sn^{4+}.[60] The peak at 162.6 eV is related to $S2p_{3/2}$ in S_2^{2-}-like chemical state.[61] The C1s XPS of GO and SnS_2/rGO are given in Figure 1d. The spectra can be fitted into four peaks for carbon atoms in different functional groups: non-oxygenated carbon (C–C 285.6 eV or C = C, 284.8 eV), carbon in C–O bonds (epoxy or hydroxyl, 286.3 eV), carbonyl carbon (C = O, 287.6 eV) and carboxyl carbon (O–C = O, 289.0 eV).[62] Note that the peak intensity of the oxygenated carbon shows a significant decrease after the solvothermal reaction, indicating a sufficient reduction of GO to rGO. The above results indicate the formation of SnS_2/rGO.

Figure 2a shows scanning electron microscopy (SEM) image of the SnS_2/rGO hybrid. Note that small SnS_2 particles are confined by rGO sheets, forming a flake-like hybrid with a size up to several micrometers. The transparent nature of rGO suggests that it is fairly thin composed probably of few-layered sheets. Transmission electron microscopy (TEM) image in Figure 2b shows that the size of SnS_2 is rather small, agreeing with its broad diffraction peaks in Figure 1a. High-resolution TEM (HRTEM) images of two typical domains (A and B) in Figure 2b are presented in Figure 2c,d. As seen from Figure 2c, SnS_2 exhibits a plate-like morphology and most of the plates align with its c-axis ([001] direction) normal to rGO sheets. HRTEM image also reveals the few-layered (<6 layers) feature of rGO as denoted by the arrow in Figure 2c. From some standing plates, the thickness of the plates is estimated to below 4 nm, corresponding to a maximum 7 layers of layered SnS_2. The lateral size of the plates is below 10 nm and the size distribution is illustrated

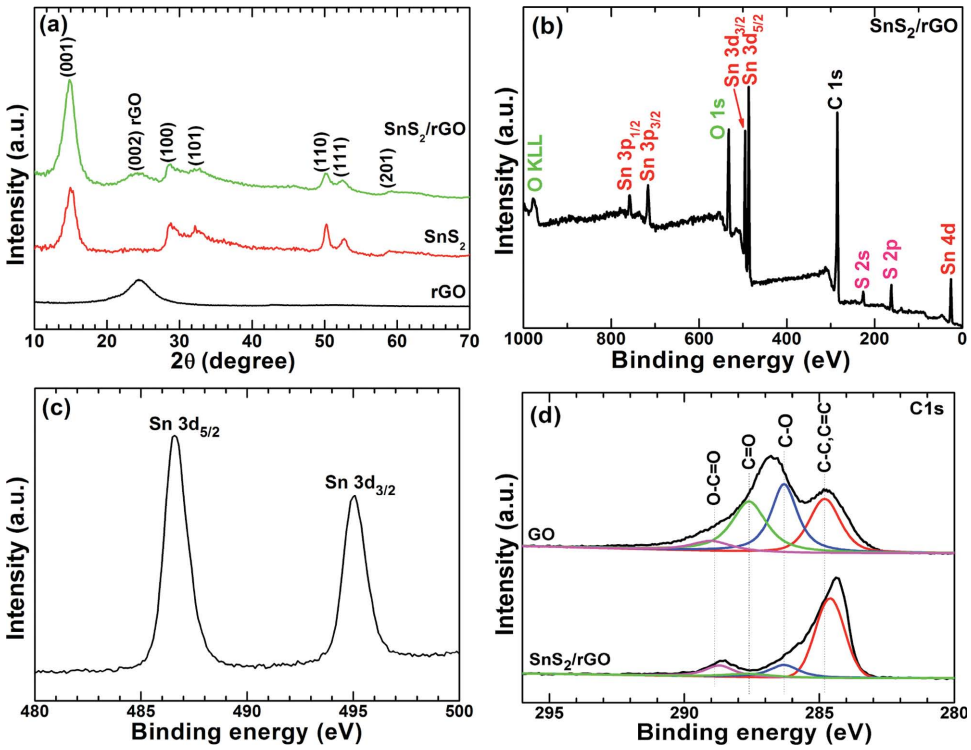

Figure 1. a) XRD patterns of SnS_2/rGO, SnS_2 and rGO; b) XPS survey of SnS_2/rGO; c) Sn3d XPS of SnS_2/rGO; d) C1s XPS of GO and SnS_2/rGO.

in the inset of Figure 2d. From atomic force microscopy (AFM) height profile in Figure 2f, the thicknesses of SnS_2 plates and rGO sheets are estimated to be <4 nm and <2 nm, respectively, in agreement with the TEM observation. As a result, a plate-on-sheet morphology has been fabricated as schematically described in **Figure 3**. In this structure, SnS_2 plates are tightly confined by rGO sheets while a large free space between the SnS_2 plates is still available for strain buffering and electrolyte penetrating.

The electrochemical performance of SnS_2/rGO was evaluated by deep galvanostatic cycling between 0.005 and 3 V. **Figure 4**a shows the voltage profiles of SnS_2/rGO in the initial 6 cycles at 100 mA g^{-1}. The first discharge (sodiation) and charge (desodiation) capacities of SnS_2/rGO are 855 and 549 mAh g^{-1}, respectively. Note that the cell experiences an activation process, during which the charge capacity gradually increases and stabilizes at 649 mAh g^{-1} after 6 cycles. The theoretical first discharge and charge capacities are 1136 and 549 mAh g^{-1} according to reactions 3,4. We notice that the stabilized charge capacity (649 mAh g^{-1}) is higher than the theoretical value of SnS_2 (549 mAh g^{-1}), implying the part decomposition of Na_2S and recovery of SnS_2 upon charge, similar to the case in Sb_2S_3.[37] Compared with SnS_2/rGO, bare SnS_2 shows a lower first charge capacity of 178 mAh g^{-1} (Figure 4b and Supporting Information Figure S3a). Bare rGO also delivers a rather lower charge capacity of only 71 mAh g^{-1} (Figure 4b and Supporting Information Figure S3c) which may comes from the binding of Na at divancancies and Stone-Wales on rGO.[20] Therefore, the remarkably increased Na-storage activity of SnS_2 in SnS_2/rGO can be attributed to the conducting and dispersing effects of rGO, not rGO itself. The first Coulombic efficiency of SnS_2 increases from 23% to 64% by rGO incorporation. On the 6th cycle, the Coulombic efficiency of SnS_2/rGO reaches ≈99%.

We notice that SnS_2 and rGO show higher first cycle loss than SnS_2/rGO. For bare SnS_2, after the first discharge process, its surface will be easily covered by solid electrolyte interface (SEI) layer formed from electrolyte decomposition due to the small size of SnS_2. The SEI layer is usually Na-ion conductive but electron insulating, which will be discussed later. Therefore, only part of the sodium can be extracted upon the subsequent charge due to the sluggish electrode reactions without electronically conductive rGO, resulting in a larger first cycle loss for bare SnS_2 than SnS_2/rGO. For bare rGO, its large first cycle loss comes from such factors as SEI formation,[16] the irreversible reaction of residual oxygen-containing groups with Na ions,[16] and the irreversible trapping of Na ions in the defective sites or amorphous regions.[20] It is possible that the exposure of the residual oxygen-containing groups and defective sites in rGO will be reduced by SnS_2 anchoring, leading to smaller first cycle loss compared with bare rGO.

After the initial activation at 0.1 A g^{-1}, the rate performance of SnS_2/rGO was evaluated by increasing the current density in steps from 0.2 to 12.8 A g^{-1}. The charge capacities at 0.2, 0.4, 0.8, 1.6, and 3.2 A g^{-1} are 582, 570, 550, 524, 501 mAh g^{-1}, respectively. At 6.4 A g^{-1}, a high charge capacity of 452 mAh g^{-1} can be achieved, corresponding to ≈70% of the charge capacity at 0.1 A g^{-1} although a 64-fold increase in current density is implemented. A chare capacity of 337 mAh g^{-1} can still be retained even at a current as high as 12.8 A g^{-1} (≈28 C). The charge capacity can be recovered to over 600 mAh g^{-1} as the current is returned to 0.1 A g^{-1}. This means that the SnS_2/rGO hybrid can tolerate high-rate cycling without damaging its

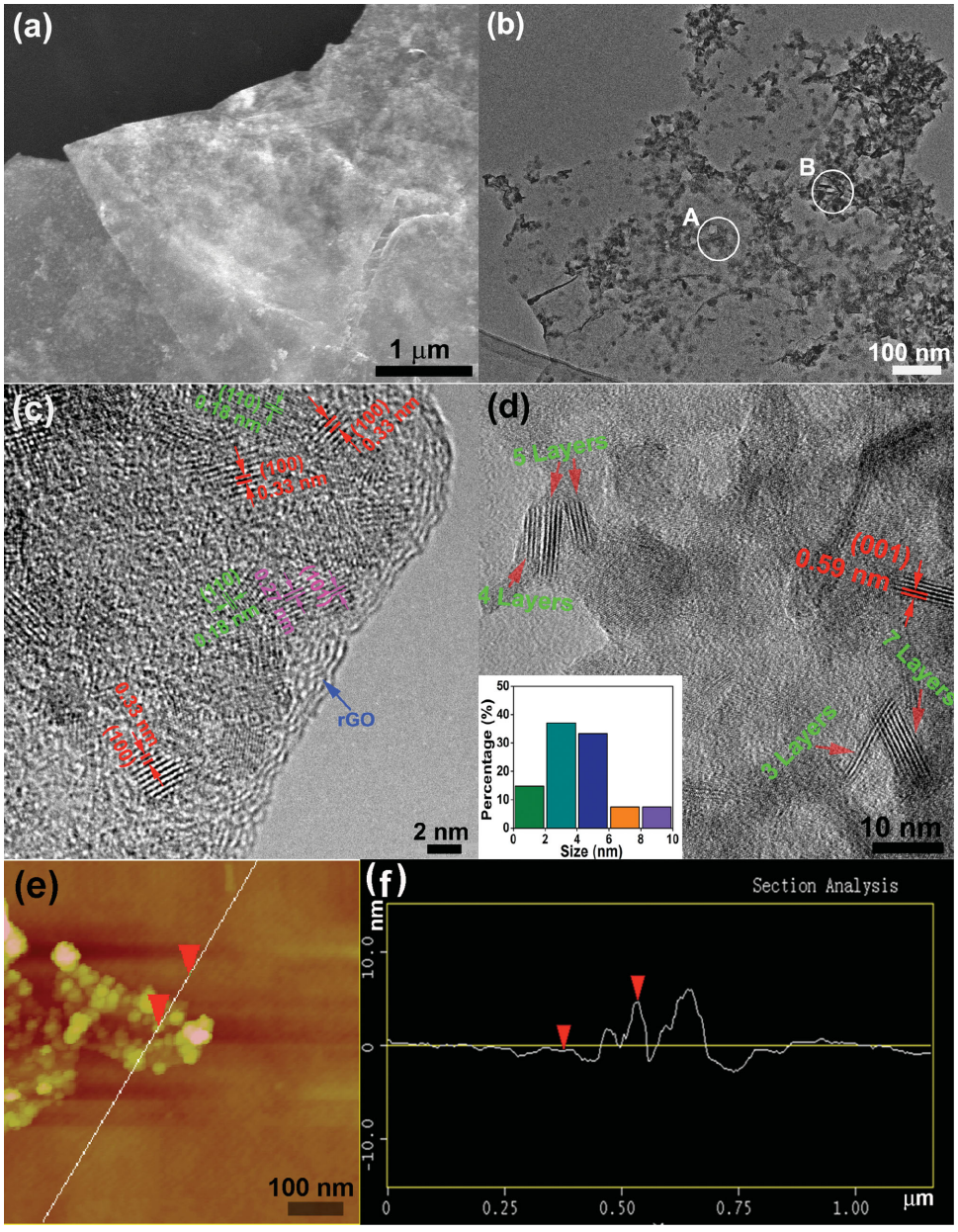

Figure 2. a) SEM image, b) TEM image, c,d) HRTEM images, and e,f) AMF image and height profile of SnS_2/rGO.

structural integrity. Figure 4d demonstrates the voltage profiles of SnS_2/rGO at various current rates, which depicts the current dependence of capacity, potential plateau and needed charge time in details. The charge plateau shows a small increase as the current increases from 0.1 to 6.4 A g^{-1}, suggesting low polarization and rapid reaction kinetics of SnS_2/rGO. Even at 12.8 A g^{-1}, we can still see well-defined charge plateau although it exhibits an obviously increased plateau potential. At such a high current, the charge process can be completed in a very short time of only 1.3 min while still yielding a moderate capacity (337 mAh g^{-1}). The superior rate capability originates from three factors: first, rGO well disperses SnS_2 plates and supplies effective 2D electronic conducting channels; second, the small lateral size and ultrathin feature of layered SnS_2 are beneficial for rapid Na-ion diffusion in bulk SnS_2 plates; third, the plate-on-sheet structure with a large free space facilitates better wetting of SnS_2/rGO by electrolyte and rapid Na-ion transport across electrode/electrolyte interface. Moreover, the rGO rich in defects is favorable for surface adsorption of Na ions.[63]

Besides rate performance, cycling stability is another important indicator for the practical applications of SnS_2/rGO. Figure 4e presents the cycling performance of SnS_2/rGO charged and discharged at 200 and 400 mA g^{-1}. After initial activation, the charge capacities of SnS_2/rGO increase to ≈590 and ≈480 mAh g^{-1}, respectively. After 300 cycles at 200 mA g^{-1}, a charge capacity of 509 mAh g^{-1} is kept for SnS_2/rGO, corresponding to capacity retention of ≈86%. The hybrid

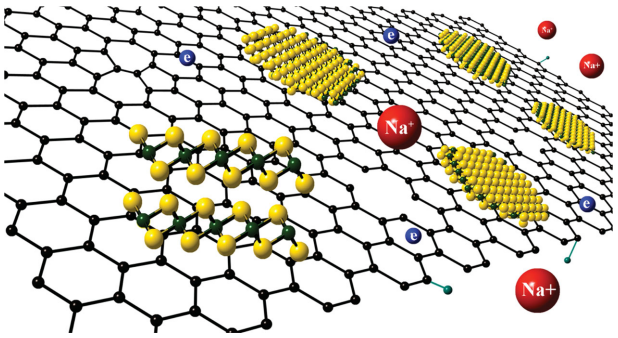

Figure 3. Schematic illustration of SnS_2/rGO.

can still exhibit a charge capacity of 360 mAh g^{-1} after 500 cycles at 400 mA g^{-1} (~75% retention), indicating excellent cycling stability. Galvanostatic cycling was also performed at 800 mA g^{-1} to evaluate high-rate cycling stability of SnS_2/rGO as shown in Figure 4f. The hybrid delivers an initial charge capacity of 470 mAh g^{-1} at 800 mA g^{-1}. The capacity retentions at 400th and 1000th are 89% and 61%, respectively. After 1000 cycles at 800 mA g^{-1} (1.8 C), a charge capacity close to 300 mAh g^{-1} is still obtainable, indicative of superior high-rate cycling stability of SnS_2/rGO. In contrast, the charge capacity of bare SnS_2 drops rapidly from a maximum 242 mAh g^{-1} to 108 mAh g^{-1} after 100 cycles even at a low current of 100 mA g^{-1} (Figure S3b, Supporting Information). The significantly enhanced cycling stability is closely related to the presence of rGO, which not only buffers the volume changes but also immobilizes the SnS_2 plates. Furthermore, the free space in the hybrid structure also effectively accommodates the volume changes. The electrochemical performance of our SnS_2/rGO is compared with that of other Sn-based anodes in the literature (**Table 1**). The electrochemical properties of two typical materials, carbon-derived

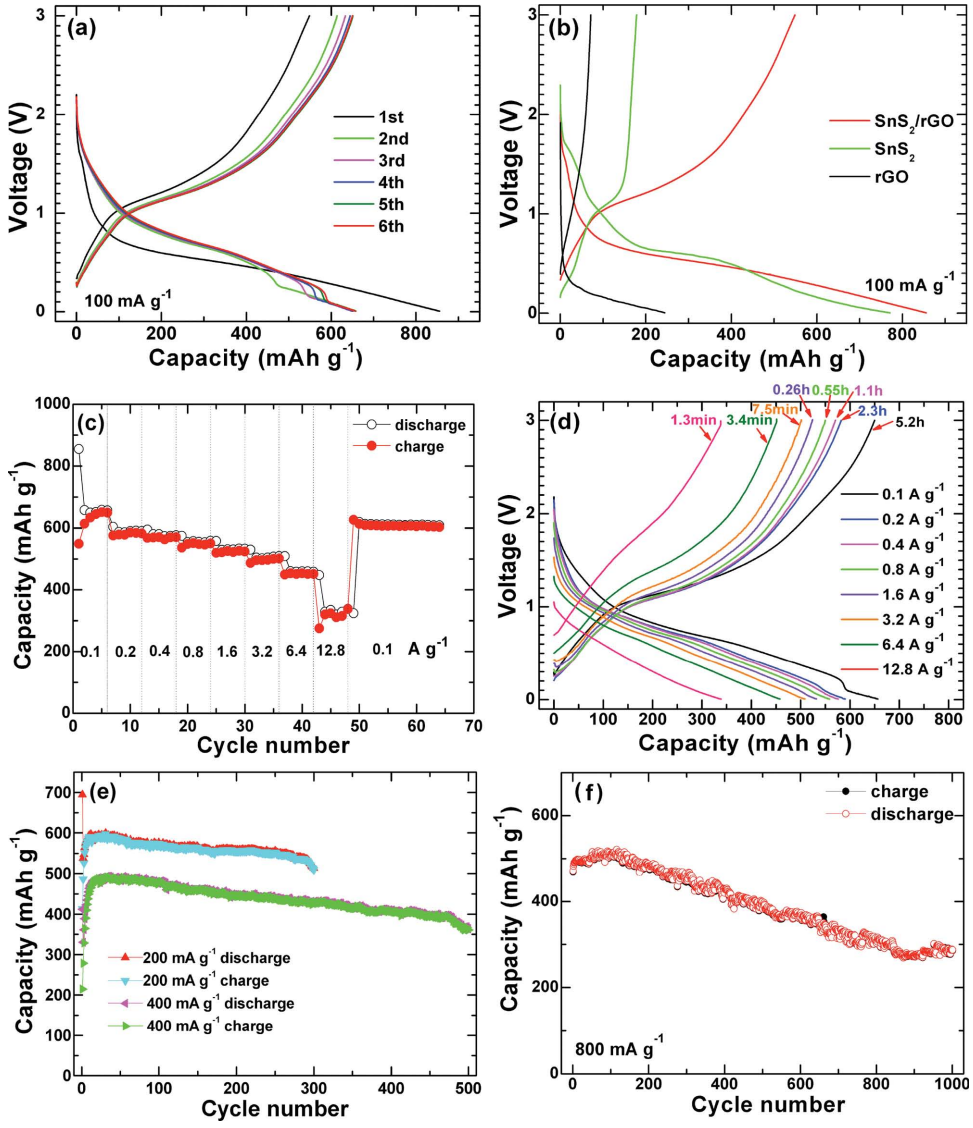

Figure 4. a) The first six voltage profiles of SnS_2/rGO at 100 mA g^{-1}; b) the first voltage profiles of SnS_2/rGO, SnS_2 and rGO; c,d) rate performance of SnS_2/rGO; e,f) cycling performance of SnS_2/rGO at 200, 400 and 800 mA g^{-1}.

Table 1. Comparison of electrochemical performance of SnS_2/rGO in this work with those of others reported in the literature.

Sample	Cycling stability				Rate capability					Reference
					Current density [mA g^{-1}]					
	Current density [mA g^{-1}]	Initial capacity [mAh g^{-1}]	Cycle number	Capacity retention	Capacity [mAh g^{-1}]					
SnS_2/rGO	**800**	**469**	**400/1000**	**89%/61%**	**100**	**400**	**6400**	**12800**		**This work**
					649	**570**	**452**	**337**		
Bio-derived carbon	100	342	290	88%	200	500	1000	2000	5000	[20]
					290	238	155	100	70	
SnSb/C	100	544	50	80%	100		500	1000		[27]
					≈540		337	274		
SnO_2/CNT	50	≈500	50	72%	25		100	250		[28]
					≈1000		≈500	≈300		
SnO_2	20	≈500	100	≈90%			–			[29]
SnS–Sn–C	100	416	150	87%	100		400	800		[30]
					485		397	348		
$Sn_{50}Ge_{25}Sb_{25}$	85	833	50	75%	850			8500		[31]
					658			381		
SnO	50	570	50	44%	100		500	1000		[32]
					≈400		200	≈150		
Sn_4P_3	100	718	100	≈90%			–			[33]
SnO_2/rGO	160	≈350	100	≈86%	40		160	640		[38]
					<600		≈350	~150		
SnO_2/rGO	100	406	150	≈81%	100		500	1000		[39]
					≈400		≈200	125		
MoS_2/rGO	25	338	20	83%	25		100	200		[48]
					240		214	173		
SnS_2/rGO	20	725	60	92%	40		160	640		[57]
					632		572	463		
SnS/rGO	30	1037	50	91%	810		7290			[58]
					492 (250th)		308 (250th)			
SnS_2/rGO	1000	594	400	84%	100		500	2000		[59]
					671		620	544		

carbon with intercalation mechanism and MoS_2/rGO with conversion mechanism, are also given for comparison. It should be addressed that the data listed in Table 1 represent the best ones reported so far. For the comparison of rate capability, the maximum applied current density is given for each work. Clearly, our SnS_2/rGO is among the best ones when comprehensively considering the capacity, cycle life, and the applied current density.

Ex situ characterization on the cycled electrodes was performed to understand the excellent electrochemical performance of SnS_2/rGO. TEM image in **Figure 5**a indicates that the original flake-like structure is generally maintained after cycling while the thickness of the flake is increased obviously. HRTEM in Figure 5b reveals the presence of well crystallized, small-sized Sn nanocrystals as marked by the green circles. It seems that the Sn crystals are surrounded by the substance with an amorphous feature. It assumes that the amorphous substance is the SEI layer resulting from the electrolyte decomposition. XPS measurements on the cycled SnS_2/rGO were conducted to confirm this assumption. In F1s spectrum of Figure 5c, the bands at 685.2 and 687.4 eV suggest the formation of NaF and organic fluorides, respectively.[64,65] As shown in Figure 5d (C1s XPS), compared with the pristine SnS_2/rGO, the cycled one displays increased peak intensity of C–O, C = O, O–C = O groups and brings a new O(C = O)O group, implying the formation of Na_2CO_3 and sodium alkyl.[64,65] XPS results confirm the formation of SEI layer.

According to Ji et al., a stable and thin SEI film is expected to form when fluoroethylene carbonate (FEC), an electrolyte additive, was used.[65] Electrochemical impedance spectroscopy (EIS) was used to reveal the nature of the SEI layer and its evolution during cycling. Figure 5e,f compares the Nyquist plots of SnS_2/rGO and

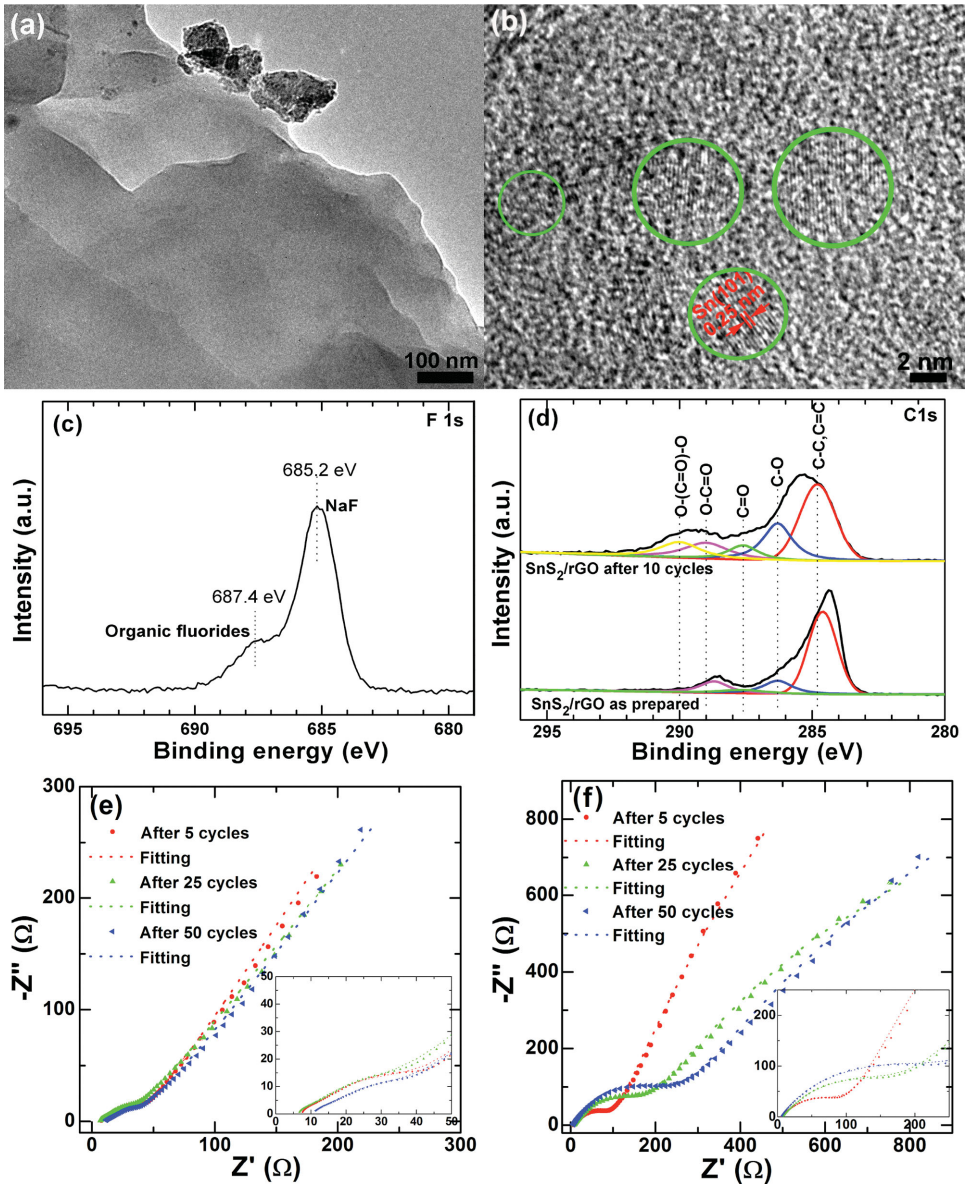

Figure 5. a,b) TEM and HRTEM images and c,d) F1s and C1s XPS of the SnS_2/rGO electrode after 10 cycles; e,f) EIS of SnS_2/rGO and bare SnS_2 after different cycles.

bare SnS_2 after different cycles. The Nyquist plots are fitted by the equivalent circuit (Figure S4, Supporting Information) and the fitting results are summarized in Table S1 (Supporting Information). The results show that the SEI film resistance (R_f) shows a small value and a slight increase upon cycling for both SnS_2/rGO and SnS_2. The corresponding constant phase element (Q_1) also exhibits a small change during cycling. The results confirm the formation of a thin and stable SEI layer induced by FEC. A stable and thin SEI layer plays a critical role in inhibiting continuous electrolyte decomposition and promoting easy Na-ion transport across the film.[65] Thus, a thin and stable SEI layer is also indispensable for stable cycling of SnS_2/rGO, in addition to buffering effect of rGO, and the free space in the hybrid.

EIS is also used to explain the different electrochemical behaviors between SnS_2/rGO and SnS_2. Of note is that, rather different behaviors in charge transfer resistance (R_{ct}) and the related constant phase element (Q_2) are observed between SnS_2/rGO and bare SnS_2. Compared with bare SnS_2, SnS_2/rGO demonstrates a much lower R_{ct} value and smaller changes in R_{ct} and Q_2. The conducting effect of rGO is responsible for the lower R_{ct} value of SnS_2/rGO, while the dispersing and immobilizing effects of rGO account for the smaller changes in R_{ct} and Q_2 during cycling. For bare SnS_2, although a thin SEI layer benefits rapid Na-ion transport, the electron transfer is yet difficult in the absence of rGO since the SEI layer is usually electronically insulating. This can explain the low Na-storage capacity of bare SnS_2 even at a low current density. For SnS_2/rGO, besides its small size and enhanced electrode wetting, the low R_{ct} value brought by rGO also contributes greatly to its superior rate performance and high-rate cycling stability. These results suggest

that the outstanding electrochemical performance of SnS_2/rGO is related both to the unique microstructure of the hybrid and to the formation of a desired SEI layer.

3. Conclusion

In summary, we fabricated a SnS_2/rGO nanohybrid by a facile one-pot solvothermal route. The hybrid consists of ultrafine (<10 nm), few-layered (≤7 layers) SnS_2 and few-layered rGO (<6 layers), forming a unique plate-on-sheet structure. The charge capacity at 100 mA g^{-1} increases from 178 mAh g^{-1} for bare SnS_2 to 649 mAh g^{-1} for SnS_2/rGO due to the dispersing and conducting effects of rGO. The hybrid can yield charge capacities of 507 and 360 mAh g^{-1}, respectively, after 300 cycles at 200 mA g^{-1} and 500 cycles at 400 mA g^{-1}. The hybrid can sustain 1000 cycles under 800 mA g^{-1} (1.8 C), maintaining a capacity around 300 mAh g^{-1}. The ultralong cycle life of SnS_2/rGO is attributed to the buffering effect of the flexible rGO and the free space in the hybrid. Besides, the formation of a stable SEI film also contributes to the excellent cycling performance by stabilizing the electrode/electrolyte interface. The hybrid can yield high charge capacities of 524, 501, and 452 mAh g^{-1}, respectively, at high current densities of 1.6, 3.2, and 6.4 A g^{-1}. Even at 12.8 A g^{-1} (28 C), it can still deliver a moderate charge capacity of 337 mAh g^{-1}. The excellent rate capability is ascribed to 2D conductive channels constructed by rGO, small lateral size and ultrathin nature of layered SnS_2, the unique hybrid structure with enhanced electrolyte penetration, and rapid Na-ion transport across the thin SEI layer. The outstanding performance of SnS_2/rGO makes it a promising anode material for Na-ion batteries.

4. Experimental Section

Materials Preparation and Characterization: Detailed description on the preparation of the SnS_2/rGO hybrid is given in the Supporting Information. The phases of the products were checked by X-ray diffraction (XRD) on a Rigaku D/Max-2550pc powder diffractometer equipped with Cu K_α radiation ($\lambda = 1.541$ Å). X-ray photoelectron spectra (XPS) were measured on a KRATOS AXIS ULTRA-DLD spectrometer with a monochromatic Al K_α radiation ($h\nu = 1486.6$ eV). The morphologies of the products were characterized by field-emission scanning electron microscope (SEM) on a FEI-sirion microscope, transmission electron microscopy (TEM) and high-resolution TEM (HRTEM) on a JEM 2100F microscope. Atomic force microscopy (AFM) image was recorded on a Vecco Multimode atomic force microscope using the tapping mode. Thermogravimetric (TG) analysis was conducted on a DSCQ1000 instrument from 35 to 800 °C at a ramp rate of 10 °C min^{-1} in air. The cycled electrodes were also characterized by XPS and TEM.

Electrochemical Measurements: The electrode slurry was made by mixing 75 wt% active material (SnS_2/rGO, SnS_2, or rGO), 15 wt% acetylene black, and 10 wt% polyacrylic acid (PAA) binder in a water/ethanol mixture (1:1 in volume) with magnetic stirring for 2 h. The working electrodes were made by spreading the slurry onto Ni foam followed by drying at 100 °C under vacuum overnight. The exact weight of all the electrodes is summarized in Table S2. CR2025-type coin cells were assembled in an Ar-filled glove box using Na foil as the counter electrode and glass fiber (Whatman GF/D) as the separator. The electrolyte was 1 M $NaPF_6$ dissolved in ethylene carbonate (EC)/diethyl carbonate (DEC) (1:1 in volume). Fluoroethylene carbonate (FEC) was used as the electrolyte additive. The volume of FEC is 5% of the total volume of EC and DEC. The cells were charged and discharged at various current densities between 0.005 and 3.0 V (vs Na/Na^+) on a Neware battery tester (Shenzhen, China). Unless otherwise stated, for SnS_2/rGO, the specific capacity was calculated based on the mass of SnS_2 and the specific current was set based on the total mass of SnS_2 and rGO. Electrochemical impedance spectroscopy (EIS) measurements were performed on a Princeton Applied Research VersaSTAT3 electrochemistry workstation with an ac voltage of 10 mV amplitude over the frequency range 10^{-3}–10^6 Hz at charge (de-sodiation) states after the cells have been cycled for desired cycles and stayed at open circuit voltage (OCV) for 10 h. All of the electrochemical measurements were performed at 25 °C.

Supporting Information

Supporting Information is available from the Wiley Online Library or from the author.

Acknowledgements

This work was supported by the National Basic Research Program of China (2013CB934001), the National Natural Science Foundation of China (No. 51101139), the Fundamental Research Funds for the Central Universities (2014XZZX002–03), Key Science and Technology Innovation Team of Zhejiang Province under Grant Number 2010R50013, and Program for Innovative Research Team in University of Ministry of Education of China (IRT13037).

Received: August 18, 2014
Revised: October 8, 2014
Published online: November 26, 2014

[1] V. Palomares, P. Serras, I. Villaluenga, K. B. Hueso, J. Carretero Gonźalez, T. Rojo, *Energy Environ. Sci.* **2012**, *5*, 5884–5901.
[2] S. W. Kim, D. H. Seo, X. H. Ma, G. Ceder, K. Kang, *Adv. Energy Mater.* **2012**, *2*, 710–721.
[3] M. D. Slater, D. Kim, E. Lee, C. S. Johnson, *Adv. Funct. Mater.* **2013**, *23*, 947–958.
[4] S. Y. Hong, Y. Kim, Y. Park, A. Choi, N. S. Choi, K. T. Lee, *Energy Environ. Sci.* **2013**, *6*, 2067–2081.
[5] V. Palomares, M. Casas Cabanas, E. Castillo Martínez, M. H. Han, T. Rojo, *Energy Environ. Sci.* **2013**, *6*, 2312–2337.
[6] P. Ge, M. Fouletier, *Solid State Ionics* **1988**, *28–30*, 1172–1175.
[7] M. M. Doeff, Y. P. Ma, S. J. Visco, L. C. De Jonghe, *J. Electrochem. Soc.* **1993**, *140*, L169–L170.
[8] D. A. Stevensa, J. R. Dahn, *J. Electrochem. Soc.* **2000**, *147*, 1271–1273.
[9] P. Thomas, D. Billaud, *Electrochim. Acta* **2002**, *47*, 3303–3307.
[10] S. Komaba, W. Murata, T. Ishikawa, N. Yabuuchi, T. Ozeki, T. Nakayama, A. Ogata, K. Gotoh, K. Fujiwara, *Adv. Funct. Mater.* **2011**, *21*, 3859–3867.
[11] R. Alcántara, G. F. Ortiz, P. Lavela, J. L. Tirado, *Chem. Mater.* **2006**, *18*, 2293–2301.
[12] Y. Matsuo, K. Ueda, *J. Power Sources* **2014**, *263*, 158–162.
[13] Z. H. Wang, L. Qie, L. X. Yuan, W. X. Zhang, X. L. Hu, Y. H. Huang, *Carbon* **2013**, *55*, 328–334.
[14] Y. L. Cao, L. F. Xiao, M. L. Sushko, W. Wang, B. Schwenzer, J. Xiao, Z. M. Nie, L. V. Saraf, Z. G. Yang, J. Liu, *Nano Lett.* **2012**, *12*, 3783–3787.
[15] H. G. Wang, Z. Wu, F. L. Meng, D. L. Ma, X. L. Huang, L. M. Wang, X. B. Zhang, *ChemSusChem* **2013**, *6*, 56–60.

[16] Y. X. Wang, S. L. Chou, H. K. Liu, S. X. Dou, *Carbon* **2013**, *57*, 202–208.
[17] A. Ponrouch, A. R. Goñi, M. Rosa Palacín, *Electrochem. Commun.* **2013**, *27*, 85–88.
[18] W. H. Li, L. C. Zeng, Z. Z. Yang, L. Gu, J. Q. Wang, X. W. Liu, J. X. Cheng, Y. Yu, *Nanoscale* **2014**, *6*, 693–698.
[19] J. Ding, H. L. Wang, Z. Li, A. Kohandehghan, K. Cui, Z. W. Xu, B. Zahiri, X. H. Tan, E. M. Lotfabad, B. C. Olsen, D. Mitlin, *ACS Nano* **2013**, *7*, 11004–11015.
[20] E. M. Lotfabad, J. Ding, K. Cui, A. Kohandehghan, W. P. Kalisvaart, M. Hazelton, D. Mitlin, *ACS Nano* **2014**, *8*, 7115–7129.
[21] Q. Sun, Q. Q. Ren, H. Li, Z. W. Fu, *Electrochem. Commun.* **2011**, *13*, 1462–1464.
[22] A. Darwiche, C. Marino, M. T. Sougrati, B. Fraisse, L. Stievano, L. Monconduit, *J. Am. Chem. Soc.* **2012**, *134*, 20805–20811.
[23] J. F. Qian, Y. Chen, L. Wu, Y. L. Cao, X. P. Ai, H. X. Yang, *Chem. Commun.* **2012**, *48*, 7070–7072.
[24] Y. J. Zhu, X. G. Han, Y. H. Xu, Y. H. Liu, S. Y. Zheng, K. Xu, L. B. Hu, C. S. Wang, *ACS Nano* **2013**, *7*, 6378–6386.
[25] L. Wu, F. Pei, R. J. Mao, F. Y. Wu, Y. Wu, J. F. Qian, Y. L. Cao, X. P. Ai, H. X. Yang, *Electrochim. Acta* **2013**, *87*, 41–45.
[26] L. Wu, X. H. Hu, J. F. Qian, F. Pei, F. Y. Wu, R. J. Mao, X. P. Ai, H. X. Yang, Y. L. Cao, *Energy Environ. Sci.* **2014**, *7*, 323–328.
[27] L. F. Xiao, Y. L. Cao, J. Xiao, W. Wang, L. Kovarik, Z. M. Nie, J. Liu, *Chem. Commun.* **2012**, *48*, 3321–3323.
[28] Y. Wang, D. W. Su, C. Y. Wang, G. X. Wang, *Electrochem. Commun.* **2013**, *29*, 8–11.
[29] D. W. Su, C. Y. Wang, H. Ahn, G. X. Wang, *Phys. Chem. Chem. Phys.* **2013**, *15*, 12543–12550.
[30] L. Wu, X. H. Hu, J. F. Qian, F. Pei, F. Y. Wu, R. J. Mao, X. P. Ai, H. X. Yang, Y. L. Cao, *J. Mater. Chem. A* **2013**, *1*, 7181–7184.
[31] B. Farbod, K. Cui, W. P. Kalisvaart, M. Kupsta, B. Zahiri, A. Kohandehghan, E. M. Lotfabad, Z. Li, E. J. Luber, D. Mitlin, *ACS Nano* **2014**, *8*, 4415–4429.
[32] M. Shimizu, H. Usui, H. Sakaguchi, *J. Power Sources* **2014**, *248*, 378–382.
[33] Y. Kim, Y. Kim, A. Choi, S. Woo, D. Mok, N. S. Choi, Y. S. Jung, J. H. Ryu, S. M. Oh, K. T. Lee, *Adv. Mater.* **2014**, *26*, 4139–4144.
[34] V. L. Chevrier, G. Ceder, *J. Electrochem. Soc.* **2011**, *158*, A1011–A1014.
[35] L. D. Ellis, T. D. Hatchard, M. N. Obrovac, *J. Electrochem. Soc.* **2012**, *159*, A1801–A1805.
[36] J. W. Wang, X. H. Liu, S. X. Mao, J. Y. Huang, *Nano Lett.* **2012**, *12*, 5897–5902.
[37] D. Y. W. Yu, P. V. Prikhodchenko, C. W. Mason, S. K. Batabyal, J. Gun, S. Sladkevich, A. G. Medvedev, O. Lev, *Nat. Commun.* **2013**, *4*, 2922.
[38] D. W. Su, H. J. Ahn, G. X. Wang, *Chem. Commun.* **2013**, *49*, 3131–3133.
[39] Y. X. Wang, Y. G. Lim, M. S. Park, S. L. Chou, J. H. Kim, H. K. Liu, S. X. Dou, Y. J. Kim, *J. Mater. Chem. A* **2014**, *2*, 529–534.
[40] Z. L. Jian, B. Zhao, P. Liu, F. J. Li, M. B. Zheng, M. W. Chen, Y. Shi, H. S. Zhou, *Chem. Commun.* **2014**, *50*, 1215–1217.
[41] M. D. Stoller, S. Park, Y. W. Zhu, J. H. An, R. S. Ruoff, *Nano Lett.* **2008**, *8*, 3498–3502.
[42] C. Lee, X. D. Wei, J. W. Kysar, J. Hone, *Science* **2008**, *321*, 385–388.
[43] S. Park, J. H. An, I. W. Jung, R. D. Piner, S. J. An, X. S. Li, A. Velamakanni, R. S. Ruoff, *Nano Lett.* **2009**, *9*, 1593–1597.
[44] G. D. Du, Z. P. Guo, S. Q. Wang, R. Zeng, Z. X. Chen, H. K. Liu, *Chem. Commun.* **2010**, *46*, 1106–1108.
[45] G. C. Huang, T. Chen, W. X. Chen, Z. Wang, K. Chang, L. Ma, F. H. Huang, D. Y. Chen, J. Y. Lee, *Small* **2013**, *9*, 3693–3703.
[46] Y. X. Wang, S. L. Chou, D. Wexler, H. K. Liu, S. X. Dou, *Chem. Eur. J.* **2014**, *20*, 9607–9612.
[47] Y. X. Wang, K. H. Seng, S. L. Chou, J. Z. Wang, Z. P. Guo, D. Wexler, H. K. Liu, S. X. Dou, *Chem. Commun.* **2014**, *50*, 10730–10733.
[48] L. David, R. Bhandavat, G. Singh, *ACS Nano* **2014**, *8*, 1759–1770.
[49] C. Q. Feng, L. F. Huang, Z. P. Guo, H. K. Liu, *Electrochem. Commun.* **2007**, *9*, 119–122.
[50] H. Liu, D. W. Su, G. X. Wang, S. Z. Qiao, *J. Mater. Chem.* **2012**, *22*, 17437–17440.
[51] R. Bhandavat, L. David, G. Singh, *J. Phys. Chem. Lett.* **2012**, *3*, 1523–1530.
[52] D. Y. Chen, G. Ji, B. Ding, Y. Ma, B. H. Qu, W. X. Chen, J. Y. Lee, *Nanoscale* **2013**, *5*, 7890–7896.
[53] D. W Su, S. X. Dou, G. X. Wang, *Chem. Commun.* **2014**, *50*, 4192–4195.
[54] J. W. Seo, J. T. Jang, S. W. Park, C. Kim, B. Park, J. Cheon, *Adv. Mater.* **2008**, *20*, 4269–4273.
[55] K. Chang, Z. Wang, G. C. Huang, H. Li, W. X. Chen, J. Y. Lee, *J. Power Sources* **2012**, *201*, 259–266.
[56] B. Luo, Y. Fang, B. Wang, J. S. Zhou, H. H. Song, L. J. Zhi, *Energy Environ. Sci.* **2012**, *5*, 5226–5230.
[57] X. Q. Xie, D. W. Su, S. Q. Chen, J. Q. Zhang, S. X. Dou, G. X. Wang, *Chem. Asian J.* **2014**, *9*, 1611–1617.
[58] T. F. Zhou, W. K. Pang, C. F. Zhang, J. P. Yang, Z. X. Chen, H. K. Liu, Z. P. Guo, *ACS Nano* **2014**, *8*, 8323–8333.
[59] B. H. Qu, C. Z. Ma, G. Ji, C. H. Xu, J. Xu, Y. S. Meng, T. H. Wang, J. Y. Lee, *Adv. Mater.* **2014**, *26*, 3854–3859.
[60] Y. Q. Lei, S. Y. Song, W. Q. Fan, Y. Xing, H. J. Zhang, *J. Phys. Chem. C* **2009**, *113*, 1280–1285.
[61] L. Zhu, D. Susac, M. Teo, K. C. Wong, P. C. Wong, R. R. Parsons, D. Bizzotto, K. A. R. Mitchell, S. A. Campbell, *J. Catal.* **2008**, *258*, 35–242.
[62] H. J. Shin, K. K. Kim, A. Benayad, S. M. Yoon, H. K. Park, I. S. Jung, M. H. Jin, H. K. Jeong, J. M. Kim, J. Y. Choi, Y. H. Lee, *Adv. Funct. Mater.* **2009**, *19*, 1987–1992.
[63] D. Datta, J. W. Li, V. B. Shenoy, *ACS Appl. Mater. Interfaces* **2014**, *6*, 1788–1795.
[64] V. Etacheri, O. Haik, Y. Goffer, G. A. Roberts, I. C. Stefan, R. Fasching, D. Aurbach, *Langmuir* **2012**, *28*, 965–976.
[65] L. W. Ji, M. Gu, Y. Y. Shao, X. L. Li, M. H. Engelhard, B. W. Arey, W. Wang, Z. M. Nie, J. Xiao, C. M. Wang, J. G. Zhang, J. Liu, *Adv. Mater.* **2014**, *26*, 2901–2908.